The Structures of Natively Assembled Clathrin Coated Vesicles

Mohammadreza Paraan[1], Joshua Mendez[2], Savanna Sharum[1], Danielle Kurtin[1], Huan He[1], and Scott M. Stagg[1,3]

Affiliations

[1] Institute of Molecular Biophysics, 91 Chieftain Way, Florida State University, Tallahassee, FL 32306.

[2] Department of Physics, 77 Chieftan Way, Tallahassee, FL 32306.

[3] Department of Chemistry and Biochemistry, 95 Chieftain Way, Florida State University, Tallahassee, FL 32306.

Abstract

Clathrin-mediated vesicle trafficking is one of the major mechanisms by which proteins and nutrients are absorbed by the cell and transported between organelles. The individual proteins comprising the clathrin coated vesicles (CCVs) include clathrin heavy chain (CHC), clathrin light chain (CLC), and a variety of adaptor protein complexes. Much is known about the structures of the individual CCV components, but data are lacking about the structures of the fully assembled complexes together with membrane and in complex with cargo. Here we determined the structures of natively assembled CCVs in a variety of geometries. We show that the adaptor β2-appendages crosslink adjacent CHC β-propellers and that the appendage densities reside almost exclusively in CCV hexagonal faces. We resolve how AP2 and other associated factors in hexagonal faces form an assembly hub with an extensive web of interactions between neighboring β-propellers and propose a structural model that explains how adaptor binding can direct the formation of pentagonal and hexagonal faces.

Introduction

Clathrin-mediated vesicle trafficking is a complex machinery in eukaryotes that is involved in most endocytic pathways (*1*), trafficking from trans-Golgi network (*2*), trafficking from endosomes(*3*), and also in the critical function of regenerating synaptic vesicles (*4-6*). The two main functions of this machinery are engaging with cargo and membrane and also generating negative curvature on membrane such that the cargo ends up in a vesicle. Both of these functions have been shown to be facilitated by the action of adaptor/accessory proteins which are often multi-functional and share overlapping functions (*7-9*). Clathrin plays a major role in organizing adaptors and cargo into spherical vesicles (*10-12*) by making geometrical cages of different sizes both *in vitro* and *in vivo (13, 14)*. Clathrin together with the adaptors AP1 and AP2 act as assembly hubs due to their multiple binding sites for other adaptor/accessory proteins (*15-17*). The dynamic assembly of clathrin-coated vesicles has been investigated by super-resolution time-resolved fluorescence microscopy (*8, 11, 18, 19*), and the self-assembly properties of clathrin have been understood by cryo-EM (*14, 20, 21*). However, it remains to be explained how clathrin assembly progresses into a closed fullerene-like cage with tight restraints on the configuration of hexagonal and pentagonal faces (*22*), in a mechanism that serves to transport cargo in lipid vesicles irrespective of cage geometry. In other words, what kind of interactions coordinate adaptor recruitment of cargo/clathrin and clathrin's lattice formation by self-association such that they do not interfere with each other.

Clathrin is a 190 kDa protein with an N-terminal WD40 β-propeller domain (residues 1-330) followed by three helical zig-zag domains in the shape of a leg (Fig. S1), and a C-terminal trimerization domain that assembles a clathrin triskelion (Fig. S1), which is the basic assembly unit of the clathrin cage. Clathrin alone can self-assemble into cages *in vitro* in acidic buffer due to the formation of multiple salt bridges between the heavy chains forming the edges of the clathrin cage. Clathrin light chain on the other hand is thought to have a regulatory role. In physiological pH, clathrin light chain has been shown to inhibit cage assembly. A mechanism was proposed in which assembly was inhibited when the CHC knee residues ($R_{1161}KKAR_{1165}$) interacted with CLC's N-terminal EED motif, which has been shown to be involved in the pH

dependence of cage assembly (*21, 23*). For proper assembly, according to this mechanism, CHC's knee domain can be bent when the interaction with CLC is absent. CLC's inhibition on assembly is removed *in vivo* by HIP1 (*24*) which interacts with the light chain N-terminal conserved sequence (20-41) via its DLLRKN-containing coiled-coil domain. Additionally, CLC also has a central heptad repeat that interacts with the CHC proximal domain, and a C-terminal domain that stabilizes the trimerization helices. It has been shown through FRET measurements that the light chain heptad repeat undergoes a conformational change upon cage assembly. Additionally, it has been shown through atomic force microscopy that the light chain rigidifies the CHC cage (*25*).

Numerous adaptor proteins link the clathrin cage to cargo and membrane. AP2 as well as AP1, AP3, AP180, HIP1, and EPSIN possess multiple linear motifs (clathrin boxes) in their C-terminal unstructured regions that bind the groove of the CHC β-propellers (*26*). AP2 is the heterotetrameric adaptor complex that is involved primarily in endocytosis and is comprised of two large subunits, the α2 and β2 adaptins, whose N-terminal domain forms the core complex together with the N-terminal domains of the two small subunits μ2 and σ2. The α2 adaptin mediates binding to membrane mainly through interactions with phosphatidylinositol-4,5-bisphosphate (PtdIns(4,5)P_2). α2 and β2 possess C-terminal appendage domains at their C-termini and clathrin box motifs that have been shown to bind clathrin (*16, 27, 28*). Although clathrin box binding sites are well known, the appendage binding site has been mapped to a broad region of the N-terminal CHC β-propeller and helical zig-zags (*29*). Since AP2 also binds other adaptor/accessory proteins as well as PI(4,5)P2 and cargo recognition peptides, these features make AP2 (and its counterpart AP1 in Golgi/endosome trafficking) the nucleator of CCV assembly and the main recruiter of clathrin. Though its binding to clathrin has been well established, it has remained unclear how AP2 can structurally organize the formation of spherical clathrin cages.

Clathrin triskelia assemble into cages with pentagonal, hexagonal, and occasionally heptagonal faces. There are always 12 pentagons in a cage in the rare cases of cages with heptagonal faces). As with any fullerene-like structure, curvature is only generated by the presence of pentagonal faces, and the diameter dictated by the number of hexagonal faces. For the clathrin cage, in any given edge, four different CHCs interact extensively along their proximal and distal domains. A 4.7 Å structure of clathrin cages was published recently that revealed that the interactions among different triskelion legs are highly conserved regardless of the cage size or face geometry (*14*). In that study, structures were determined of *in vitro* assembled cages together with the β2-appendage domains of AP2, but notably, they did not observe the β2-appendage density. All adaptor-clathrin interactions have been mapped to the N-terminal domain of clathrin, a region that is far from the extensively interacting proximal and distal domains. Thus, a remaining question for the field is what is the interplay between adaptor binding and the generation of cages of given diameters? How are the number of pentagonal and hexagonal faces determined? Here using cryo-EM, we have determined the structures of natively assembled CCVs that include clathrin, adaptors, accessory proteins, and cargo. Our structures show a number of previously unresolved features including adaptor β2-appendages that crosslink adjacent CHC β-propellers. Remarkably, the appendage densities reside almost

exclusively in hexagonal faces, and by performing a focused alignment and classification, we resolve how AP2 and other associated factors in hexagonal faces form an assembly hub with an extensive web of interactions between neighboring β-propellers. These observations lead us to propose a structural model that explains how adaptor binding can direct the formation of pentagonal and hexagonal faces.

Results

Natively assembled CCVs assume 5 different cage geometries including one not thought to be possible.

Clathrin-coated vesicles were purified from bovine brains in conditions that ensured CHC cages do not disassemble during purification. SDS-PAGE gels showed bands that corresponded to clathrin heavy chain and light chain and adaptor subunits (Fig. S2A). The identities of these proteins and other accessory and cargo proteins were determined by mass spectrometry (Fig. S2A). This showed that the adaptors AP2 and AP180 were highly abundant followed by AP1 and AP3. Other essential accessory proteins were present in the CCVs including AP2-associated kinase 1 (AAK1), EPSIN, HIP1, and amphiphysin. Besides AP2 and AP180, all the other essential components of synaptic vesicles (SVs) (*30*) were present in the spectra including: VAMP2 (R-SNARE protein), synaptophysin (VAMP2 chaperone and inhibitor), synapsin (localizes SVs to the

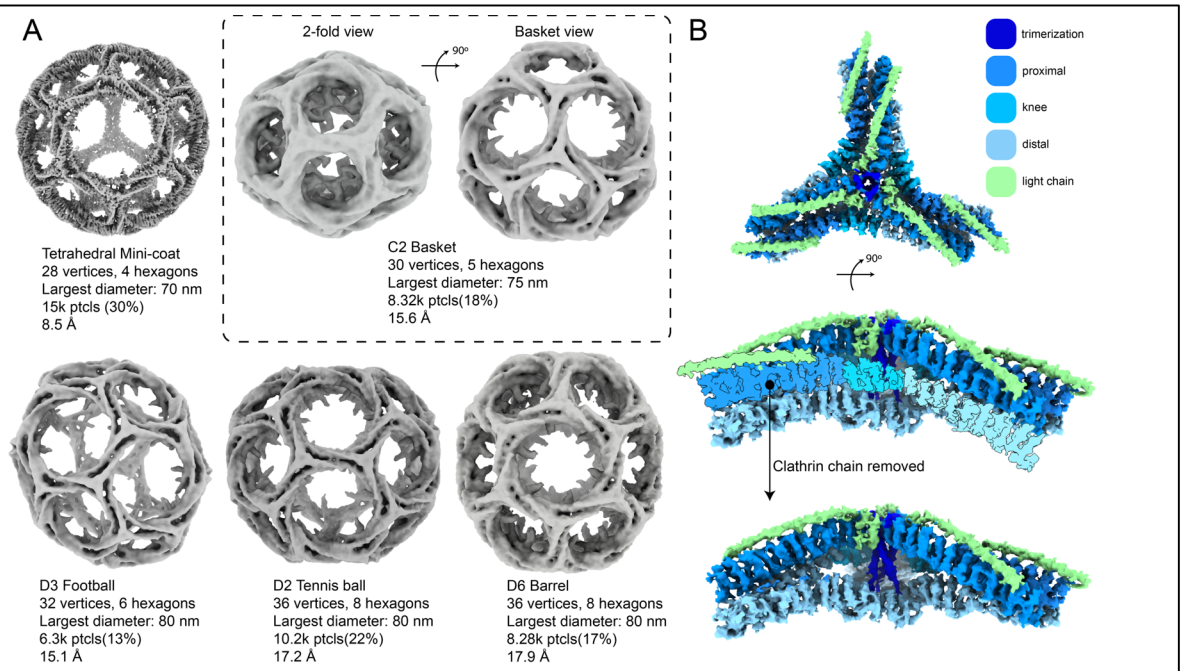

Figure 1. Single particle refinement of CCVs. A) Refinement of CCVs into 5 different cage geometries. The tetrahedral mini-coat has the highest resolution among the geometries. The C2 basket is a novel geometry represented in two views in the dashed panel. The largest cage is the D6 barrel. B) Clathrin-focused subparticle refinement of the mini-coat asymmetric vertex further improves the resolution. Top: asymmetric vertex refinement with colors representing different domains, resolution: 6.3 Å ($FSC_{0.143}$). Middle: Side view of the vertex. Bottom: Side view with one CHC and CLC removed to show the trimerization helices.

synapse pool), sodium-potassium ATPase pump and H^+ ATPase pump, and neurotransmitter transporters (Fig. S2A). SV-related proteins had the highest number of unique peptides and

total normalized spectra in the mass spectrometry analysis reflecting their higher concentration in the purified CCVs, and these results are consistent with the synaptic vesicle protein composition that was identified by Takamori *et al.* (*31*). Other identified proteins include syntaxin 1 and 2 (plasma membrane), syntaxin 7 (early endosome, late endosome), and syntaxin 16 (*trans*-Golgi network).

The natively assembled CCVs were prepared for cryo-EM and a single particle cryo-EM dataset was collected resulting in 80k CCV particles (Fig. S2B). These were subjected to Relion's ab initio model generation (*32*) with a target of 4 models. This resulted in four CCV structures with complete cages and unique symmetries including the mini-coat (tetrahedral, 28 triskelions), football (D3, 32 triskelions, also known as sweet potato (*14*)), tennis ball (D2, 36 triskelions), and D6 barrel (D6, 36 triskelions), (Fig. 1A, Fig. S3A). However, after inspection of the individual particles it was clear that there were more geometries present in the dataset. Therefore, the cages were subjected to multiple rounds of competitive 3D classification where the particles that were already assigned to one class were further classified. This led to the identification of a subset of particles that form a previously undescribed geometry with C2 symmetry and 30 triskelions that we are calling the C2 basket (Fig. 1A). The mini-coat, football, tennis ball, and barrel structures match four of the cage geometries that were recently reported by Morris *et al*. (*14*) from *in vitro* reconstituted clathrin cages where they used a library of pre-generated cage geometries to sort their particles into the representative cage structures. This indicates that the cellular processes that assemble CCVs are similar to clathrin cages generated by reconstitution. However, there are a few exceptions; with our data-driven model generation approach, we were not able to unambiguously generate the C1 cage that Morris *et al.* observed by refining against pre-generated cage geometries. It is possible that the C1 cages are in our dataset, but they are likely such low abundance that we cannot unambiguously identify their presence. Another difference is that our largest identified cage (36 triskelions) is the smallest among 8 reported cages by Cheng *et al*. (*13*) that were purified as intact CCVs similar to our approach. Although intact CCV sample preparations follow the same ultracentrifugation protocols with slight modifications, the low abundance of cages larger than 36 triskelions in our sample and the lack of cages smaller than 36 triskelions in their sample indicates that either the source tissues differ in some way or that a subtlety in methods leads to the enrichment of smaller or larger CCVs. We have high confidence that our CCVs are representative of synaptic vesicles due to the abundance of SV proteins identified by mass spectrometry. We also confirmed the presence of vesicles inside the cages by collecting a tomogram of a field of CCVs on the same grid that we performed the single particle analysis on. This showed that vesicles were present in all the different CCV sizes (Fig. S4). The membrane is quite dense and to be loaded with membrane proteins and the inside of the vesicle is also very dense. This is consistent with the model of Takamori *et al.* (*31*) whose mass spectrometry studies of synaptic vesicles showed that the SV membrane is packed with membrane proteins. The smaller the CCVs get, the more dense it becomes inside the vesicles until the membrane and core have about equal density. There is a dense spherical core of density even in the smallest CCVs (Fig S4, top row).

The C2 basket CCV that we observe by cryo-EM is novel in two ways: first, it has not been reconstructed before in cryo-EM datasets, and second, its existence was ruled out by a cage

geometry prediction model developed by Schein (*22*) and utilized by Morris *et al*. (*14*) in structure determination. This model uses a so-called head-to-tail exclusion rule to find possible cage geometries given the number of vertices. The rule predicts that cages with too much dihedral angle discrepancy that would otherwise cause the polygonal faces to be non-planar are unlikely to form. According to this model, fullerene-like cages with 30 vertices are not permitted at all. In contrast, our C2 structure consists of 30 vertices, 12 pentagons, 5 hexagons, and 45 edges. Although this structure violates the head-to-tail exclusion rule, it follows Euler's polyhedron formula which governs the geometry of closed polyhedrons. The specific region of this geometry that violates the head-to-tail rule consists of 4 adjacent pentagons with 5 mutually-shared edges (Fig. S5A). Two of these pentagons each contain two vertices where the rule is violated and thus there should be excessive torsion (Fig. S5A). This explains the slightly weaker density for the CHC chains highlighted in Figure. S5A.

The refined clathrin cages were further subjected to subparticle refinement (*33*) to improve the resolution of the clathrin layer. The asymmetric vertex (surrounded by hexagonal-pentagonal-pentagonal or HPP faces) of the mini-coat refined to 6.3 Å ($FSC_{0.143}$) (Fig. S3B) overall with some areas as high as 4.6 Å (Fig. 1B, Fig. S3D), while its pentagonal and hexagonal faces refined to 9.1 and 8.3 Å, respectively (Fig. S3B). The other cage geometries also produced subparticle reconstructions for the HPP asymmetric vertex with resolution ranging between 8-9 Å (Fig. S3B,C). This held true for the asymmetric vertex of the C2 basket structure as well (Fig. S3B,C, Fig. S5B).

Atomic modeling of the asymmetric vertex structure reveals interactions of the QLMLT motif of the CHC and the stabilizing interactions of the CLC with CHC.

Atomic models were built of the mini-coat HPP asymmetric vertex. The model by Morris *et al*. (*14*) that was built into their consensus C3 vertex (PPP) was docked into our C1 vertex. In this rigid-body fit, the edge of the vertex that is between two pentagonal faces exhibits an accurate fit, while the two other edges with one hexagonal face do not enclose the model starting at positions close to the knee domain. This discrepancy is due to our map deriving from the asymmetric vertex while theirs is from the symmetric one and is consistent with observations that the knee domain changes conformation to make hexagonal and pentagonal faces (*14*) while the proximal domain is stabilized by CLC. Using the asymmetric vertex structure from the mini-coat, a homology model of the bovine CHC and CLC was built and refined to our map (Fig. 2A, Fig. S6). The C-terminal trimerization domain residues plus 15 novel residues following them were built *de novo* including QLML residues of the QLMLT motif (Fig. 2B, Fig. S6E) (*34*). The QLMLT motif is critical for Hsc70 binding and clathrin uncoating (*34*). These residues follow the final C-terminal helix of CHC at the trimerization domain which sits on top of three distal legs crossing below making a triangle (Fig. S7A). We show that each QLML motif then extends from the trimerization helix and interacts with two crossing distal legs (Fig. S7B). In this way, the center of a triskelion stabilizes three other CHC chains that pass under it and each end up in

a face around the vertex. These trimerization:distal leg interactions contribute to the interactions between adjacent CHCs, and help explain why region is targeted by the ATPase Hsc70 during cage disassembly through interaction with the QLMLT motif.

Another important interaction that happens at the center of the vertex is between CHC and CLC. Three C-terminal helices of CLC form a U-shaped domain that lies against CHC residues at the trimerization domain burying hydrophobic residues along the interface and stabilizing the trimerization domain (Fig. S8). This interaction is similar to what was reported by Morris et al., but with small differences in the atomic model. Our model contains a small helix that is modelled as a loop in the previously published PDB-6SCT (*14*). Our change orients a number of hydrophobic residues to be packed against the trimerization domain (Fig. S8).

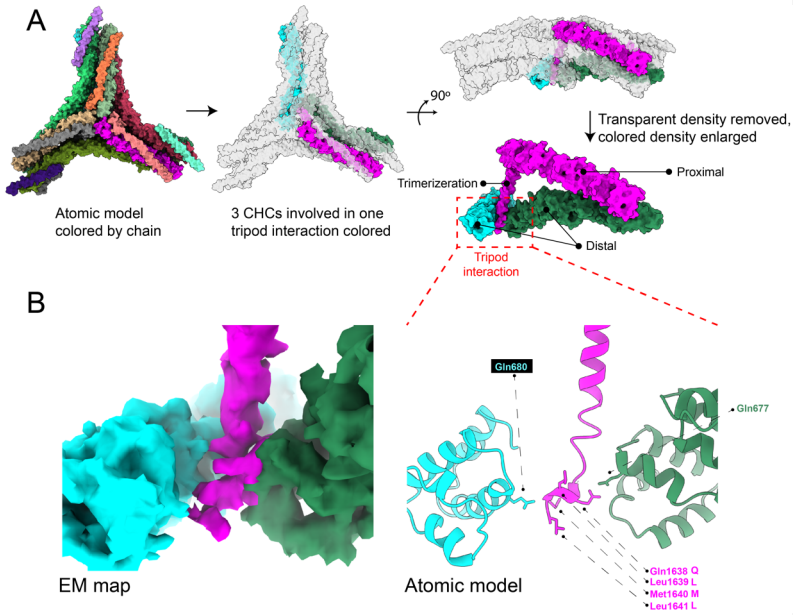

Figure 2. Atomic modeling of the tripod interactions (colored by chain). A) The left panel shows the full vertex atomic model. The middle panel shows the same atomic model with only 3 CHCs colored. The top right panel is a side view of the model, and the bottom right panel shows only the 3 interacting CHCs. B) The right panel shows the EM density map for the tripod interaction. The left panel show the position of the QLML residues of the QLMLT motif extending down from the trimerization helix.

Adaptor appendage densities attached to CHC β-propellers are enriched in hexagonal faces. Inspection of the CHC β-propeller densities in the mini-coat reconstruction revealed that there are three copies of a density consistent with the AP2 β2-appendage domain that reside exclusively in the hexagonal faces and not in the pentagonal faces (Fig. 3). We identify the density as belonging to the AP2 β2-appendage for three reasons. First, the density fits the β2-appendage crystal structure very well (*35*) (Fig. 3A). Secondly, AP2 β2-appendage has been shown experimentally to bind and assemble clathrin cages whereas the other appendage domain-containing adaptors have not (*28*). Finally, our CCVs are highly enriched in synaptic vesicles (Fig. S2), and one of the main mechanisms of SV recycling is with clathrin mediated endocytosis from the plasma membrane which requires AP2. Docking the crystal structure of the β2-appendage in the observed densities aligns residues Y815 of the β-sandwich sub-domain and Y888 of the platform sub-domain (*16, 36*) with two neighboring β-propeller domains from two different CHCs (Fig. 3A) effectively crosslinking the two CHCs. For each of the three β2-appendages, one of the two sub-domain densities connects down to the body of the adaptor which allowed us to orient the domains. In the tetrahedral mini-coat, the hexagonal faces lie on three-fold axes of symmetry, and three appendages can easily be accommodated by the six β-

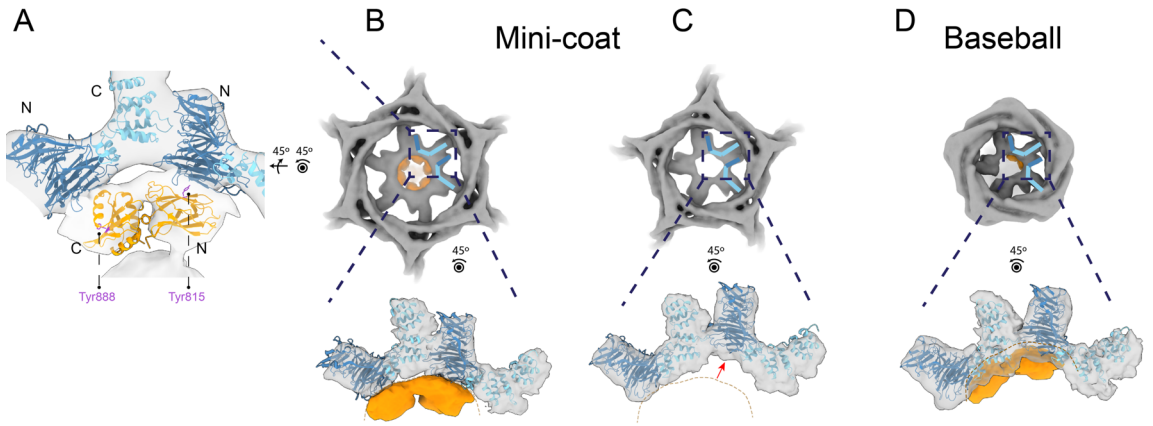

Figure 3. Three-way interaction between β-propeller and β2-appendage and β-propeller and ankle. β-propeller, ankle, and β2-appendage densities and crystal structures are shown in dark blue, light blue, and orange, respectively. A) Cross-linking of two β-propellers by a β2-appendage domain. Fitted crystal structures are PDB ids 1BPO (clathrin) and 1E42 (β2-appendage), respectively. B) All hexagonal faces of the mini-coat contain three copies of the β2-appendage density. The dashed boxes indicate zoomed views. The dashed line in the bottom panel roughly outlines the interface between β-propellers and β2-appendage and is used as reference for panels C and D. C) Pentagonal faces of the mini-coat only have densities for clathrin. Bottom panel shows the movement of the right clathrin leg compared to its position in a hexagonal face as shown in B. D) larger cages like the D2 baseball have β2-appendage densities in their pentagonal faces, unlike the mini-coat. However, the position of the β2-appendage in a pentagonal face is different than its position in a hexagonal face (compare B and D).

propellers in the hexagonal face. The other cage geometries also have an abundance of β2-appendage as well as other extra densities in their hexagonal faces (Fig. S9). With the larger geometries, weak appendage densities could also be observed in pentagonal faces that have multiple neighboring hexagonal faces as discussed in the following sections.

Compared to the reconstituted clathrin cage reconstructions by cryo-EM (*14, 20, 37*), our structures have strong densities for the CHC β-propeller domains for all geometries, and they are in contact with the neighboring CHC ankle domain. This is consistent with the observation that the β2-appendages crosslink the β-propellers to the ankle domains in native CCVs. These contacts are different between the hexagonal and pentagonal faces, but consistent across all cage geometries (Fig. 3B,C bottom panels). The differences lie in the region of the β-propeller that is interacting with the ankle and the relative distances and orientations of two neighboring β-propellers. Due to these differences, in pentagonal faces of large cages like D2 baseball, β2-appendage density is displaced (Fig. 3D) presumably to maintain the same contacts with the β-propellers as those in hexagonal faces (Figure 3A,B).

Pentagonal faces with adaptor appendages have at least two neighboring and consecutive hexagonal faces.

Unlike hexagonal faces where adaptor appendages are found in abundance in all geometries, appendage densities in pentagonal faces depend on their neighboring faces. In the five resolved cage geometries, there are three possible configurations of neighboring faces for each pentagonal face (Fig. 4A-C). The first configuration has two non-neighboring hexagonal faces

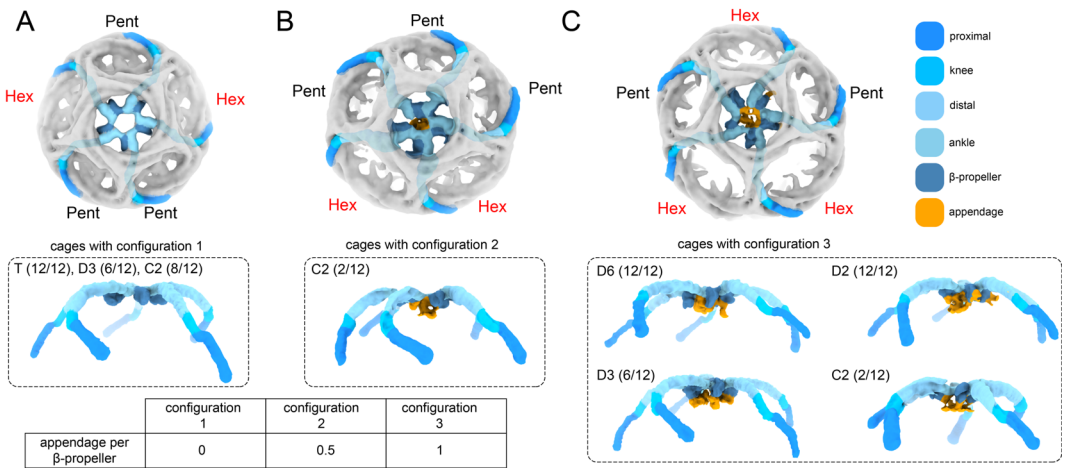

	configuration 1	configuration 2	configuration 3
appendage per β-propeller	0	0.5	1

Figure 4. Three different configurations of neighboring faces for a pentagonal face in all geometries and their relation to the population of adaptor appendages in the pentagonal face (colored by domain as in Figures 1 and 3). Fractions show the number of pentagonal faces in each configuration out of the 12 total pentagonal faces. A) Top panel: Configuration 1 for faces neighboring a pentagonal face. The neighboring faces are indicated with Pent and Hex. The CHC chains with β-propellers in the central pentagonal face are traced using the color code. Bottom panel: The same CHCs traced in the top panel are shown in a side view with no appendages present. Geometries with configuration 1 are indicated (T, D3, C2). The organization of the top and bottom panels are the same for B and C. B) Configuration 2. This configuration is unique to C2 basket. The bottom panel shows that some β-propellers are engaged with adaptor appendages. C) Configuration 3. The four different geometries indicated in the bottom panel accommodate configuration 3 in which all β-propellers are engaged with adaptor appendages. The table shows relationship between configuration and approximate percentage of β-propellers in the central pentagonal face of that configuration that are engaged with adaptor appendages.

and appears in the mini-coat, football, and basket geometries (Fig. 4A, top panel). This configuration has no associated adaptor appendages in the pentagonal faces (Fig. 4A, bottom panel). The mini-coat pentagonal faces are comprised entirely of this configuration, which explains why no appendage densities are observed in the pentagonal faces for that geometry. In the football geometry six of the twelve pentagonal faces are in this configuration, and remarkably none of those faces contain appendage densities. The same is true for the basket geometry. The second configuration is unique to the basket geometry and has two neighboring hexagonal faces that adjoin each other (Fig. 4B, top panel). In this configuration two of the β-propellers in the pentagonal face are interacting with adaptor appendages while the remaining 4 β-propellers show no appendage densities (Fig. 4B, bottom panel). The third configuration has three total hexagonal faces two of which adjoin each other and this appears in the barrel, football tennis ball, and basket geometries (Fig. 4C, top panel). In this configuration all β-propellers in the pentagonal faces interact with adaptor appendages (Fig. 4C, bottom panel). This observation clearly shows that the presence of appendages in pentagonal faces depends on having adjacent hexagonal faces where two of the hexagonal faces adjoin each other (Figure

4B,C). This configuration, by necessity, becomes more common with large cages, and accordingly, we observe more appendage densities in pentagonal faces with larger and larger cages (Fig. 4). These results suggest that a cluster of adaptors in adjoining hexagonal faces also engage their neighboring pentagonal β-propellers.

Subparticle refinement reveals AP2 core density.

Since adaptor densities were present in our CCVs but we were only resolving the appendages, we performed subparticle refinement on the hexagonal faces to better resolve the adaptors. 60k hexagonal face subparticles were generated from 15k mini-coat CCVs. A focused classification scheme (Fig. 5A, Fig. S10) was used that focused on alignment and classification of the density below the CHC layer (Fig. 5B,C). In this refinement, a spherical focus mask was created that enclosed the CHC ankle and β-propeller and the β2 appendages and the smeared out spherical AP2 density below them. After multiple rounds of classification and removal of poorly aligning particles, this revealed a class that showed adaptor density consistent with AP2 in the center of the hexagonal faces (Fig. 5B,C). Although the AP2 density was relatively low-resolution, it is distinguished by 3 features: 1) the core AP2 complex in the open conformation (PDB-2XA7, (7)) fits inside the corresponding AP2 density (Fig. 5B), 2) AP2 density makes two

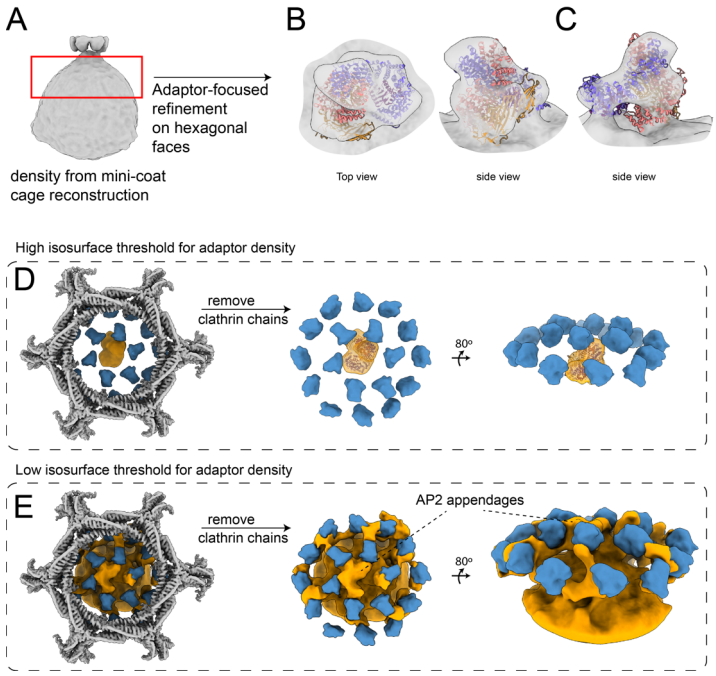

Figure 5. Adaptor focused refinement revealing AP2 density and a crowded web of appendages (colored by domain as in Figures 3, and 4). A) β2-appendages of one hexagonal face and averaged-out density from the mini-coat cage refinement, red box indicates the volume that was further resolved in subparticle alignment. B) the result of subparticle alignment reveals a density resembling the AP2 core. The crystal structure of open AP2 conformation is fitted inside. C) AP2 density at a slightly higher isosurface threshold than B to emphasize the two connecting densities. D) Relative positions of clathrin hexagonal face (gray), clathrin β-propellers (blue), and AP2 core densities (orange) are shown. The clathrin hexagonal face density is removed to show the proximity of AP2 to 18 β-propellers. E) Same views of D are shown here at a lower isosurface threshold to show the interaction web of β-propellers and the cluster of densities formed around AP2.

points of contact with the density below (Fig. 5C) corresponding to the reported α and μ interactions with PI(4,5)P2 and cargo peptides, respectively, 3) appendage densities connect AP2 to CHC β-propeller domains (Fig. 5E). Additionally, at a lower isosurface threshold, multiple densities emerge that engage the β-propellers of neighboring pentagonal faces (Fig. 5E). These observations are consistent with the idea that hexagonal adaptor clusters can engage more than just six hexagonal β-propellers. Our hexagonal face map shows that a total of 18 β-propellers are engaged with a cluster of proteins centered on the AP2 adaptor (Fig. 5D,E).

Discussion

Structure determination of natively assembled CCVs has revealed many new insights into the interplay between adaptor binding and clathrin cage assembly. CCVs are highly heterogeneous in size, shape, and composition especially with respect to the membrane and cargo proteins (Fig. S2B). Nonetheless, using cryo-EM we were able to classify the cages into five discrete geometries that represent the majority of CCVs we imaged. Using subparticle reconstruction, we determined the structure of the most abundant vertex which is asymmetric and formed from the intersection of two pentagonal faces and one hexagonal face. This structure confirmed that the interactions that Morris *et al. (14)* observed in their reconstituted clathrin cages were conserved in our natively assembled coats. Similarly to their study, our structure also showed that the CLC C-terminal domain stabilizes the tripod domains that are critical for CHC trimerization. A unique feature of our structure was the C-terminal residues of the CHC trimerization domain that stabilize the pair-wise interactions of the three distal legs that pass below the center of the vertex (Fig. 2, Fig. S7). The trimerization helices extend a bit past this region partially exposing the QLMLT motif that is recognized by Hsc70 (*34*). These observations explain how Hsc70 can compete with the tripod/distal domain interaction to destabilize cages.

One of the most striking features of the structures we observed was the enrichment of adaptor densities in the hexagonal faces of the CCV structures. In our most abundant cage, the mini-coat, there were strong densities for AP2 β2-appendages exclusively in the hexagonal faces with no noticeable density in the pentagonal faces. Based on our reconstructions, we estimate that there is around one AP2 per hexagonal face in the mini-coat CCVs. This estimate is derived in two ways. First, in the clathrin-focused subparticle refinement, the relative density value for the appendage domains is less than half of that of clathrin and it only appears in the hexagonal faces indicating an occupancy of between 1 and 2 adaptors per hexagonal face. Secondly, when we do adaptor focused subparticle refinement, we only observe one AP2 core density per hexagonal face after classification. Every hexagonal face is occupied with AP2 densities, so for the mini-coat, this observation suggests that there are around four AP2 molecules per CCV.

As the cages increased in diameter, adaptor density began to appear in the pentagonal faces, but only for faces that were bounded by two adjoining hexagonal faces (Fig. 4). We also discovered that individual appendage domains crosslink the two β-propellers of two neighboring CHCs, which in turn stabilizes a previously uncharacterized interaction between the β-propeller of one CHC and the ankle of its neighboring CHC (Fig. 3). In this way the binding of a single AP2 ties together two triskelions and promotes cage assembly. This observation also

explains why reconstructions of *in vitro* reconstituted cages lacking β2-appendages do not show the same ubiquitous β-propeller-ankle interaction that we observe. When we performed an asymmetric subparticle focused refinement on the hexagonal faces, we resolved the AP2 core and a whole network of interacting densities that link the hexagonal face β-propellers to the 12 CHC β-propeller domains in neighboring faces (Fig. 5). In this way AP2 and other associated factors can serve as a hub linking cargo binding, adaptor assembly, and clathrin assembly.

All of these observations have led us to propose a model for how adaptor binding drives the formation of discrete cage geometries. It is well-established that adaptors like AP2 drive curvature on membranes (*10*). Our data demonstrate that β2-appendages are enriched in hexagonal faces and crosslink neighboring clathrin triskelia thereby promoting the assembly of hexagonal faces. However, for the formation of a closed cage there should be a mechanism that explains how pentagonal faces are formed in the two modes of assembly: constant area and constant curvature (*11, 38*). In the constant curvature model, pentagonal faces would form in membrane regions lacking adaptor clusters in order to accommodate membrane curvature. For the constant area model, CCVs start out as a flat hexagonal lattice, and triskelia have to be removed by Hsc70/auxillin to convert hexagonal faces to pentagonal ones (*39-41*). Our data suggest the presence of an adaptor cluster in the center of hexagonal faces that ties together the 18 surrounding β-propellers and their associated triskelia (Fig. 6 blue) preventing their removal. In this view, these triskelia would remain even if the tripod interactions were disturbed temporarily by Hsc70/auxilin. This means that the only triskelia available for removal would be the distant ones that are not interacting with the adaptor cluster (Fig. 6 red). Thus, in the neighboring hexagonal faces, there is only one triskelion per face that is not engaged in any adaptor hub interactions (Fig. 6, magenta and red). If all of those triskelia were removed by Hsc70/auxillin (Fig. 6, green), then the adaptor cluster would give rise to a hexagon surrounded by six pentagons thus accommodating a curved membrane. In order to make larger cages, more hexagonal faces must be maintained via additional adaptor clusters. Thus, in our model, the positioning of the 12 pentagons that are required for the generation of a closed geometrical lattice are not determined by the geometrical constraints of clathrin but rather the positioning of adaptors. This central role of adaptors in generating clathrin geometries is supported by our observation of the C2 basket, which should be unlikely to form based on clathrin interactions

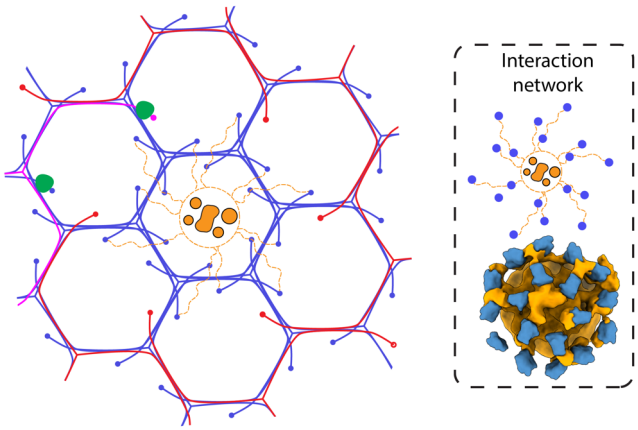

Figure 6. Model for adaptor cluster mediated organization of pentagonal and hexagonal faces (colored by domain as in previous figures). Auxilin is represented by green blobs sitting on top of β-propellers. Clathrin chains in red and magenta are not interacting with the adaptor cluster and hence can be removed. The orange adaptor cluster and the blue clathrin chains are interconnected with dashed lines. The schematic view is representing by the map shown in Figure 5E, dashed box.

alone. In this way, our model unifies the literature on CCV assembly by describing clusters of adaptors as the central machinery for curvature generation and CHC cage assembly.

Accession codes

All cryo-EM maps and structures are being deposited in the Electron Microscopy Data Bank and Protein Data bank with IDs xxx.

Acknowledgements

The authors acknowledge the use of instruments at the Biological Science Imaging Resource supported by Florida State University and NIH grants S10 RR025080 and S10 OD018142. The work presented was supported by the NIH grant R01GM108753 and funds from Florida State University.

Methods

Purification

All the following steps were done at 4°C. 120g of cow brain purchased from Pel-Freez Biologicals was homogenized in MES buffer (100mM MES, 1 mM EGTA, 0.5 mM MgCl2, pH 6.7) (*42*) plus 2 protease inhibitor cocktail tablets using an industrial blender (Final volume 300 ml). The homogenate was centrifuged at 17k *g* and the supernatant was transferred and centrifuged at 56k *g*. The pellet from that run was resuspended in MES buffer plus 12.5% w/v of each sucrose and ficoll and then homogenized again using the blender. The homogenate was spun at 43k *g* to pellet large microsomes. The supernatant was transferred and spun at 100k *g*. The pellet was resuspended in MES buffer and spun at 17k *g* to remove any remaining unwanted large lipids. The intact clathrin coated vesicles (two tubes of 7.5 ml) were then spun on an 8% sucrose cushion dissolved in MES buffer made with D_2O (2.5 ml, added to the bottom of the sample) at 116k *g* to separate out similar-sized uncoated vesicles. The pellet was resuspended in MES buffer at a concentration of 6.5 mg/ml.

Mass spectrometry

Protein digestion

Cut gel bands were de-stained with a wash buffer (50% aqueous acetonitrile with 50 mM ammonium bicarbonate) and cut into ~ 1 mm gel pieces and dried by incubation with acetonitrile followed by SpeedVac (Thermo Fisher Scientific). Digestion buffer (10% aqueous acetonitrile with 50 mM ammonium bicarbonate) was added to rehydrate the dried gel pieces, which subsequently were reduced with 0.5 mM TCEP (tris(2-carboxyethyl)phosphine, Sigma-Aldrich, catalog #: C4706, St. Louis, MO) and alkylated with 1 mM IAA (iodoacetamide, Sigma-Aldrich, catalog #: I1149, St. Louis, MO). Then trypin (Thermo Fisher Scientific, catalog #: 90058, Waltham, MA) was added to a final concentration of 0.005 µg/µL, and the mixture was incubated at 37°C overnight. Digestion was quenched by adding 0.5% formic acid aqueous solution and the supernatant was collected. The residual gel pieces were dried by incubation

with acetonitrile and the supernatant was collected. Combined supernatant containing tryptic peptides was dried in a SpeedVac.

For the in-solution protein trypsin digestion, 24.5 µL of the digestion buffer (10% aqueous acetonitrile with 50 mM ammonium bicarbonate) was added to 0.5 µL of the crude CCV sample. The mixture was then reduced with 0.5 mM TCEP, alkylated with 1 mM IAA and digested with 0.005 µg/µL trypsin at 37°C for 3 hr. The digestion was quenched by adding 0.5% formic acid aqueous solution and the tryptic peptide mixture was dried in a SpeedVac.

Tryptic peptides separation and detection

The peptide mixture was re-dissolved in 0.1% aqueous formic acid and separated by nano-liquid chromatography (nLC) with an Easy Nano LC II system (Thermo Fisher Scientific) with a 100 µm x 2 cm trap column (easy column, catalog # SC001 Thermo Fisher Scientific) and a 75 µm x 10 cm C18AQ analytical column (Thermo Fisher Scientific). Mobile phase compositions are A (0.1% aqueous formic acid) and B (99.9% acetonitrile and 0.1% formic acid). For the crude CCV sample, a linear gradient from 5% to 35% B over 2 hr was performed with a flow rate of 300 nL/min. For gel band samples, the linear gradient was from 5% to 35% B over 1 hr. Eluate was on-line ionized by nano-electrospray ionization (nESI) with a spray voltage of 2.2 kV and detected by a Hybrid Velos LTQ-Orbitrap Mass Spectrometer (MS) (Thermo Fisher Scientific). Both nLC and MS were controlled by the Xcalibur software (Thermo Fisher Scientific). The precursor ions were detected with a mass resolution of 60 K (at *m/z* of 800 Da) and Automatic Gain Control (AGC) of 1.00e+6 in the Orbitrap. Centroided data-dependent MS^2 was carried out on the top 10 most abundant precursor ions with collisional induced dissociation (CID) in the LTQ with AGC of 1.00e+4.

Data Analysis

Acquired Xcalibur.raw files were analyzed by Proteome Discoverer software (version 1.4) with a Sequest HT search engine (Thermo Fisher Scientific) against a *Bos taurus* protein fasta database with dynamic modification of methionine oxidation and static modification of cysteine carbamidomethylation. The search result was further validated and visualized with Scaffold software (version 4.3.4, Proteome Software Inc., Portland, OR).

Cryo-EM data collection and preliminary processing

3 µl of sample was applied to thick C-flat grids (CF-2/2-4C-T-5), blotted (blotting time 4s, blotting force 2) and plunged in liquid ethane using a Mark IV vitrobot (chamber humidity 100% at 4°C). Movie frames were collected using Leginon for automated data acquisition on a Titan Krios equipped with a K3 direct electron detector, at 33k magnification, super-resolution mode with a pixel size of 1.37Å, a total dose of 40.98 $e^{-}/Å^{2}$, and a defocus range of 3-5 microns. 800 micrographs were obtained after motion correction and dose weighting using MotionCorr2. Contrast transfer function was estimated using CTFFIND v4. CCV particles were picked using FindEM template picking in Appion, resulting in a total of 80k CCV particle images (894-pixel box size). FSC was generated using even and odd masked half maps, and the local resolution for the mini-coat vertex was calculated using monores .

Cage Structure determination

The pool of 80k CCV particle images was 2D-classified using cryoSPARC leaving 60k particles which were then 3D-classified using Relion and cisTEM into 5 different clathrin cage geometries:

1) *mini-coat* (15k particles, T symmetry, 28 triskelions, 24 C1 (HPP) vertices, 4 C3 vertices, 4 hexagonal faces)
2) *C2 basket* (8.32k particles, C2 symmetry, 30 triskelions, 22 C1 HPP vertices, 4 C3 vertices, 4 C1 vertices, 5 hexagonal faces)
3) *football* (6.3k particles, D3 symmetry, 32 triskelions, 24 C1 HPP vertices, 2 C3 vertices, 6 C1 HHP, 6 hexagonal faces)
4) *D6 barrel* (8.28k particles, D6 symmetry, 36 triskelions, 24 C1 HPP vertices, 12 C1 HHP vertices, 8 hexagonal faces)
5) *tennis ball* (10.2k particles, D2 symmetry, 36 triskelions, 24 C1 HPP vertices, 12 C1 HHP vertices, 8 hexagonal faces)

The C2 basket geometry was delineated from a pool of football particles that were classified into two classes using cisTEM, with the D3 map as the initial model and no symmetry applied. As a last step, to prepare cage maps and metadata (Euler angles) for subparticle analysis, the Euler angles were refined in cisTEM with no symmetry applied, then the maps were reconstructed with symmetry in Relion to enable consistent subtraction of projections from images during the subparticle analysis (refer to the next section) and also to adjust the grayscale of the maps to that of the particle images.

Subparticle analysis

For each of the five cage geometries, three sets of subparticles were defined: vertices, pentagonal faces, and hexagonal faces. There are 12 pentagonal faces in any of the given cage geometries, but the number of hexagonal faces increases with the diameter of the cage. Vertices are divided to three subcategories. The most abundant vertex geometry in any cage geometry is one made by two pentagonal faces and one hexagonal face (HPP). The other two vertex geometries (PPP, HHP) are either absent in some of the cages or vary in number between different cages.

All the subparticles were extracted using the *localized_reconstruction.py* script (*33*) implemented in Scipion and adopted to work with Relion3 rather than Relion1.4. The input parameters for the localized reconstruction script included: 1) STAR file of refined particle images of a cage, 2) a map of the corresponding cage, missing the subparticle of interest, to be projected and subtracted from particle images, 3) C1 symmetry for both particles and subparticles, 4) coordinates of the *center* of the subparticles in *CMM* format, determined such that the clathrin heavy chain part of the subparticle is always centered in its new subparticle box, 5) subparticle box size of 600 pixels (unbinned), 6) Z-axis alignment enabled. The subparticles were extracted from the parent cage particle image. Stacks of both subtracted and non-subtracted subparticles images were created, both unbinned and binned by 2. The subtracted images were only used for high resolution refinement of clathrin at vertices. First, subparticles were re-centered to eliminate centering errors of the extraction step using

cryoSPARC 2D classification and alignment. Then subparticles were refined in cryoSPARC against an initial model extracted from the corresponding cage map. The only symmetry applied for subparticle refinement was C3 for PPP vertices.

Heavy chain refinement to high resolution

cryoSPARC maps and metadata were exported and refined further in cisTEM. To achieve a higher resolution, we focused on the asymmetric vertex of the mini-coat, since the mini-coat CCV reconstruction had the highest resolution among the different geometries. At this point the images were unbinned and the super resolution pixels were being used in refinement. After refinement in cisTEM, vertex map and metadata were exported to Relion for CTF refinement where per particle defocus and beam tilt were refined. Afterwards, the final map was generated by refinement in cisTEM.

Adaptor classification and analysis

After refinement of clathrin heavy chain (and light chain) of hexagonal and pentagonal faces of each cage geometry in cryoSPARC, the faces were classified individually in Relion into two classes. Centered at β-propellers, a spherical mask with a diameter of 196 Å was applied such that the hypothetical space occupied by adaptors below β-propellers and the inner distal and proximal clathrin legs in that face were all weighted by one, and everything outside the spherical mask weighted by zero with a Gaussian falloff at the edge of the mask. In that manner, 10 hexagonal and pentagonal subparticles were classified to 20 classes initially.
60k hexagonal face particle images from the mini-coat were first classified to two classes. Each class contained 30k particles and both resolved a similar density that resembled the AP2 core density. Therefore, each of the classes were classified further into two classes. Again, the same density was resolved with slightly more features and in a seemingly different orientation. Two more classification steps revealed the AP2 core density presented in Figure 5. A similar hierarchical classification scheme was carried out for the pentagonal face of the mini-coat. Unlike the hexagonal face, no adaptor density was resolved for the pentagonal face.

Model Building

An initial model for *Bos taurus* CHC and CLC was created from the previously published cryo-EM clathrin model (6SCT (*14*)) from *Sus scrofa.* The sequence for CHC in *Bos taurus* is identical to *Sus scrofa*. The CLC sequences are 96.5% identical, and the nonidentical *Sus scrofa* residues were converted to *Bos taurus* ones by mutating them in UCSF Chimera . The homology model for a single leg of the triskelion was rigid body fit into our asymmetric vertex map. The density for hydrophobic interactions between the heavy chain and the light chain in conjunction of other bulky side chain densities were in good agreement with the model. Structural differences were noted for CLC residues 188-228 between our map and the porcine map, so these were remodeled in 6 residues steps using Rosetta enumerative sampling (RosettaES) and residues 189-199 from 6SCT model as initial model. On each step, a larger section of the map was segmented allowing for the 6 residues to be model into the new density. Additionally, compared to the porcine map, we resolved additional CHC tripod residues. Using RosettaES and residues 1596-1626 from 6SCT, 15 additional residues were modeled. For the remaining legs of the triskelion, the leg structure that we modeled as described above was rigid body fit into the

corresponding densities. Since our vertex density was not symmetric only the proximal domains of the model fit perfectly into the density. The atoms lying outside of the map were moved into the density using Rosetta torsion space refinement that generally preserves secondary structure and side chain interactions. After the complete vertex model was generated, it was refined using Rosetta cryo-EM refinement protocol resulting in three thousand refined models. The models were sorted by total energy and the model with the lowest energy was selected for further refinement using phenix.real_space_refine .

Molecular graphics images were produced using the UCSF Chimera package from the Computer Graphics Laboratory, University of California, San Francisco (supported by NIH P41 RR-01081).

References

1. M. Kaksonen, A. Roux, Mechanisms of clathrin-mediated endocytosis. *Nat Rev Mol Cell Biol* **19**, 313-326 (2018).
2. K. Kim, S. K. G. Gadila, Cargo trafficking from the trans-Golgi network towards the endosome. *Biol Cell* **108**, 205-218 (2016).
3. J. P. Chamberland, L. T. Antonow, M. Dias Santos, B. Ritter, NECAP2 controls clathrin coat recruitment to early endosomes for fast endocytic recycling. *J Cell Sci* **129**, 2625-2637 (2016).
4. N. L. Kononenko *et al.*, Clathrin/AP-2 mediate synaptic vesicle reformation from endosome-like vacuoles but are not essential for membrane retrieval at central synapses. *Neuron* **82**, 981-988 (2014).
5. N. Jung, V. Haucke, Clathrin-mediated endocytosis at synapses. *Traffic* **8**, 1129-1136 (2007).
6. Y. Mori, S. Takamori, Molecular Signatures Underlying Synaptic Vesicle Cargo Retrieval. *Front Cell Neurosci* **11**, 422 (2017).
7. L. P. Jackson *et al.*, A large-scale conformational change couples membrane recruitment to cargo binding in the AP2 clathrin adaptor complex. *Cell* **141**, 1220-1229 (2010).
8. B. T. Kelly *et al.*, Clathrin adaptors. AP2 controls clathrin polymerization with a membrane-activated switch. *Science* **345**, 459-463 (2014).
9. S. E. Miller *et al.*, CALM regulates clathrin-coated vesicle size and maturation by directly sensing and driving membrane curvature. *Dev Cell* **33**, 163-175 (2015).
10. R. Lundmark, S. R. Carlsson, Driving membrane curvature in clathrin-dependent and clathrin-independent endocytosis. *Semin Cell Dev Biol* **21**, 363-370 (2010).
11. B. L. Scott *et al.*, Membrane bending occurs at all stages of clathrin-coat assembly and defines endocytic dynamics. *Nat Commun* **9**, 419 (2018).
12. V. Haucke, M. M. Kozlov, Membrane remodeling in clathrin-mediated endocytosis. *J Cell Sci* **131**, (2018).
13. Y. Cheng, W. Boll, T. Kirchhausen, S. C. Harrison, T. Walz, Cryo-electron tomography of clathrin-coated vesicles: structural implications for coat assembly. *J Mol Biol* **365**, 892-899 (2007).

14. K. L. Morris *et al.*, Cryo-EM of multiple cage architectures reveals a universal mode of clathrin self-assembly. *Nat Struct Mol Biol* **26**, 890-898 (2019).
15. L. M. Traub, Common principles in clathrin-mediated sorting at the Golgi and the plasma membrane. *Biochim Biophys Acta* **1744**, 415-437 (2005).
16. E. M. Schmid *et al.*, Role of the AP2 beta-appendage hub in recruiting partners for clathrin-coated vesicle assembly. *PLoS Biol* **4**, e262 (2006).
17. A. Pechstein *et al.*, Regulation of synaptic vesicle recycling by complex formation between intersectin 1 and the clathrin adaptor complex AP2. *Proc Natl Acad Sci U S A* **107**, 4206-4211 (2010).
18. A. Grassart *et al.*, Actin and dynamin2 dynamics and interplay during clathrin-mediated endocytosis. *J Cell Biol* **205**, 721-735 (2014).
19. J. Y. Toshima *et al.*, Spatial dynamics of receptor-mediated endocytic trafficking in budding yeast revealed by using fluorescent alpha-factor derivatives. *Proc Natl Acad Sci U S A* **103**, 5793-5798 (2006).
20. A. Fotin *et al.*, Molecular model for a complete clathrin lattice from electron cryomicroscopy. *Nature* **432**, 573-579 (2004).
21. J. D. Wilbur *et al.*, Conformation switching of clathrin light chain regulates clathrin lattice assembly. *Dev Cell* **18**, 841-848 (2010).
22. S. Schein, Architecture of clathrin fullerene cages reflects a geometric constraint--the head-to-tail exclusion rule--and a preference for asymmetry. *J Mol Biol* **387**, 363-375 (2009).
23. J. A. Ybe *et al.*, Clathrin self-assembly is regulated by three light-chain residues controlling the formation of critical salt bridges. *EMBO J* **17**, 1297-1303 (1998).
24. V. Legendre-Guillemin *et al.*, Huntingtin interacting protein 1 (HIP1) regulates clathrin assembly through direct binding to the regulatory region of the clathrin light chain. *J Biol Chem* **280**, 6101-6108 (2005).
25. P. N. Dannhauser *et al.*, Effect of clathrin light chains on the stiffness of clathrin lattices and membrane budding. *Traffic* **16**, 519-533 (2015).
26. J. Muenzner, L. M. Traub, B. T. Kelly, S. C. Graham, Cellular and viral peptides bind multiple sites on the N-terminal domain of clathrin. *Traffic* **18**, 44-57 (2017).
27. W. Hao, Z. Luo, L. Zheng, K. Prasad, E. M. Lafer, AP180 and AP-2 interact directly in a complex that cooperatively assembles clathrin. *J Biol Chem* **274**, 22785-22794 (1999).
28. L. A. Wood, G. Larocque, N. I. Clarke, S. Sarkar, S. J. Royle, New tools for "hot-wiring" clathrin-mediated endocytosis with temporal and spatial precision. *J Cell Biol* **216**, 4351-4365 (2017).
29. B. Greene, S. H. Liu, A. Wilde, F. M. Brodsky, Complete reconstitution of clathrin basket formation with recombinant protein fragments: adaptor control of clathrin self-assembly. *Traffic* **1**, 69-75 (2000).
30. S. E. Miller *et al.*, The molecular basis for the endocytosis of small R-SNAREs by the clathrin adaptor CALM. *Cell* **147**, 1118-1131 (2011).
31. S. Takamori *et al.*, Molecular anatomy of a trafficking organelle. *Cell* **127**, 831-846 (2006).
32. J. Zivanov *et al.*, New tools for automated high-resolution cryo-EM structure determination in RELION-3. *Elife* **7**, (2018).

33. S. L. Ilca *et al.*, Localized reconstruction of subunits from electron cryomicroscopy images of macromolecular complexes. *Nat Commun* **6**, 8843 (2015).
34. I. Rapoport, W. Boll, A. Yu, T. Bocking, T. Kirchhausen, A motif in the clathrin heavy chain required for the Hsc70/auxilin uncoating reaction. *Mol Biol Cell* **19**, 405-413 (2008).
35. E. ter Haar, A. Musacchio, S. C. Harrison, T. Kirchhausen, Atomic structure of clathrin: a beta propeller terminal domain joins an alpha zigzag linker. *Cell* **95**, 563-573 (1998).
36. M. A. Edeling *et al.*, Molecular switches involving the AP-2 beta2 appendage regulate endocytic cargo selection and clathrin coat assembly. *Dev Cell* **10**, 329-342 (2006).
37. A. Fotin *et al.*, Structure of an auxilin-bound clathrin coat and its implications for the mechanism of uncoating. *Nature* **432**, 649-653 (2004).
38. D. Bucher *et al.*, Clathrin-adaptor ratio and membrane tension regulate the flat-to-curved transition of the clathrin coat during endocytosis. *Nat Commun* **9**, 1109 (2018).
39. X. Wu *et al.*, Clathrin exchange during clathrin-mediated endocytosis. *J Cell Biol* **155**, 291-300 (2001).
40. E. Eisenberg, L. E. Greene, Multiple roles of auxilin and hsc70 in clathrin-mediated endocytosis. *Traffic* **8**, 640-646 (2007).
41. Y. Chen *et al.*, Dynamic instability of clathrin assembly provides proofreading control for endocytosis. *J Cell Biol* **218**, 3200-3211 (2019).
42. B. M. Pearse, M. S. Robinson, Purification and properties of 100-kd proteins from coated vesicles and their reconstitution with clathrin. *EMBO J* **3**, 1951-1957 (1984).